Insights into the micromechanics of stress-relaxation and creep behaviours in the aortic valve

Afshin Anssari-Benam[1,*], Hazel R. C. Screen[2] and Andrea Bucchi[1]

[1] Cardiovascular Engineering Research Laboratory (CERL),
School of Mechanical and Design Engineering,
University of Portsmouth,
Anglesea Road,
Portsmouth PO1 3DJ
United Kingdom

[2] Institute of Bioengineering,
School of Engineering and Materials Science,
Queen Mary, University of London,
Mile End Road,
London E1 4NS
United Kingdom

[*] Address for correspondence: Afshin Anssari-Benam,
Cardiovascular Engineering Research Laboratory (CERL),
School of Mechanical and Design Engineering,
University of Portsmouth,
Anglesea Road,
Portsmouth PO1 3DJ
United Kingdom

Tel: +44 (0)23 9284 2187
Fax: +44 (0)23 9284 2351
E-mail: afshin.anssari-benam@port.ac.uk

Word count (Introduction to Conclusion): 7302

1

Abstract

Viscoelastic attributes of the aortic valve (AV) tissue are, in part, reflected in stress-relaxation and creep behaviours observed *in vitro*. While the extent of AV time-dependent behaviour under physiological conditions is not yet fully understood, *in vitro* the tissue exhibits clear stress-relaxation but minimal creep under equi-biaxial loading, in contrast to uniaxial loading where creep is evidently exhibited. Tissue-level stress-relaxation behaviour follows the form of (single and double) *Maxwell*-type exponential decay relaxation modes, and creep occurs in the form of exponential primary followed by linear secondary creep modes. This paper aims to provide an explanation for these behaviours based on the AV microstructural (i.e. fibre-level) mechanics. The kinematics of AV microstructural reorganisation is investigated experimentally using confocal microscopy to track the interstitial cell nuclei as markers of AV microstructural reorganisation under uniaxial loading. A theoretical framework is then applied to describe the experimentally observed kinematics in mathematical terms. Using this framework it is shown that at the microstructural level, AV stress-relaxation and creep behaviours both stem from the same dissipative kinematics of fibre-fibre and fibre-matrix interactions, that occur as a consequence of microstructural reorganisation due to the applied tissue-level loads. It is additionally shown that the proposed dissipative kinematics correctly predict the nature of relaxation and creep behaviours, i.e. the type and the number of modes involved. Further analysis is presented to demonstrate that the origin of the minimal creep behaviour under equi-biaxial loading can be explained to stem from tissue-level loading boundary conditions. These key findings help to better understand the underlying causes of AV stress-relaxation and creep behaviours *in vivo*, and why these may differ from the behaviours observed under non-physiological *in vitro* loading.

Keywords: Aortic valve, microstructure, viscoelasticity, stress-relaxation, creep, collagen fibre kinematics.

Insights into the micromechanics of stress-relaxation and creep behaviours in the aortic valve

1. Introduction

The time-dependent nature of the mechanical behaviour of valvular tissues including the aortic valve (AV) has been documented in the form of stress-relaxation and creep (Anssari-Benam et al. 2011a; Sauren et al. 1983; Stella et al. 2007), as well as the rate-dependency of the stress-strain curves (Anssari-Benam et al. 2011a; 2017; 2018). The contribution of structural components of the valve to its tensile deformation behaviour has been well-developed and incorporated into various computational and continuum-based models of the AV including the role of collagen fibres (Billiar and Sacks 2000), their angular distribution (Billiar and Sacks 2000, Sacks 2003), elastin network (Anssari-Benam and Bucchi 2018) and the rate-dependent behaviour of the glycosaminoglycans or GAGs (Anssari-Benam et al. 2017; 2018). However, how these structural components contribute to and facilitate AV stress-relaxation and creep behaviours is considerably less well-known.

Stress-relaxation behaviour is postulated to be a particularly important mechanical attribute of the native valve, as the structural durability of the AV is thought to be linked with its ability to dampen the transient stresses created by sudden changes in pressure gradient at the systolic phase of each cardiac cycle (Sacks 2001; Robinson and Tranquillo 2009). Indeed, calcification and structural failure of substitute valves may be a consequence of the poor capacity of the substitute structures to mimic the stress-relaxation properties of the native valve (Sacks 2001; Robinson and Tranquillo 2009). By contrast, the native AV is known not to exhibit creep under physiological loading conditions *in vivo*, which may too be a contributing factor to the long-term structural integrity and functional longevity of the native valve. These seemingly uncoupled, and perhaps even contradictory, attributes of the AV motivate studying and understanding the contributory structural mechanism(s) that regulate those behaviours.

Tissue level *in vitro* stress-relaxation and creep behaviours of heart valves have been characterised within the criteria of linear (Anssari-Benam et al. 2011a; 2015; Liao et al. 2007) and quasi-linear viscoelasticity (Sauren et al. 1983; Anssari-Benam 2014), amongst other frameworks, with varying success. The general consensus, however, from an

experimental point of view is that the AV tissue appears to exhibit *Maxwell*-type exponential decay of stress during the relaxation process, both under uniaxial (Anssari-Benam et al. 2011a) and biaxial (Stella et al. 2007; Huang and Shadow Huang, 2015) loading. In particular, under uniaxial loading conditions, relaxation of the AV tissue at lower strains was observed to follow a single *Maxwell* decay mode in both the radial and circumferential directions, whereas at higher strains it switched to double *Maxwell* decay modes (Anssari-Benam et al. 2011a). The consensus surrounding the AV creep behaviour is more scarce, as there are not many studies in the literature concerning AV creep characteristics. We have previously shown the expression of two creep modes, namely primary and secondary creep, under uniaxial loading *in vitro* (Anssari-Benam et al. 2011a). However, studies investigating the creep behaviour of valvular tissues under equi-biaxial loading have reported negligible levels of creep (Stella et al. 2007; Liao et al. 2007).

Not much attempt has been made to date to explain these complex and seemingly contradictory behaviours based on the underlying AV microstructural mechanism(s). Of the few existing studies, Liao et al. (2007) noted a reduction in collagen fibril D-spacing during relaxation in valvular tissues, and a hypothesis is presented that a "fibril-level locking mechanism" exists within the tissue that would allow for stress-relaxation under constant strain, but would inhibit creep under constant stress (Stella et al. 2007; Liao et al. 2007). This hypothesis appears to indicate that relaxation and creep mechanisms are uncoupled, and have distinct structural causes. Differently from this hypothesis, we postulate that the two phenomena are coupled and originate from the same structural mechanism, which can be explained at the microstructure (i.e. fibre) level, and the determining factor for manifestation of relaxation or creep at the tissue level is only the applied boundary condition.

In this paper, we investigate our presented hypothesis above and demonstrate that the dissipative kinematics arising as a result of the reorganisation of the AV microstructure, in the form of fibre rotation and sliding under the application of tissue-level loads, is the underlying mechanism that results in both the observed tissue-level stress-relaxation and creep behaviours. In order to demonstrate this premise, we first experimentally verify the existence of these kinematics under a wide-range of uniaxial tissue level loads/deformations, and then underline a theoretical mathematical criterion to link the observed kinematics to the origins of stress-relaxation and creep behaviours at the tissue

level. We mathematically demonstrate how the applied boundary conditions determine the form of tissue-level response, i.e. stress relaxation or creep, and further show that the minimal levels of AV creep under biaxial loading is a direct result of the tissue-level biaxial loading boundary condition, which may also explain why the tissue does not creep *in vivo*.

2. Experimental procedure

In order to characterise the reorganisation of the AV microstructure and quantify fibre kinematics, we utilised the aortic valve interstitial cell (AVIC) nuclei as fiducial micro-markers for tracking fibre movements during stress-relaxation and creep tests. AVICs are known to be bonded to the fibrous structure of the valve (Shadow Huang et al. 2007; Meng et al. 2008) and tracking their movement may be used as a measure of the reorganisation of the AV microstructure (Lewinsohn et al. 2011; Anssari-Benam et al. 2012). For the purpose of this study, AV specimens were prepared from porcine hearts obtained from animals aged between 18 and 24 months, from a local abattoir within two hours of slaughter.

The technique for tracking the movement of the AVIC nuclei was developed and presented in detail in a series of our previous studies (e.g. see Lewinsohn et al. 2011 and Anssari-Benam et al. 2012). In brief, the three AV leaflets were dissected from the aortic root (Figure 1a) and maintained in Dulbecco's Modified Eagle's Medium (DMEM, Sigma, Poole, UK), at 25° C. From each leaflet, a 5 mm wide circumferential or radial strip was excised from the central (belly) region, as shown in Figure 1a. After excision, the strip specimens were incubated in Acridine Orange (5 mM in DMEM, Invitrogen, Oregon, USA) for 1 hour at 25° C, to stain the cell nuclei. Each specimen was then briefly rinsed in DMEM prior to testing. The prepared specimens were secured within a custom-made uniaxial loading rig, placed on the stage of a confocal laser scanning microscope (UltraView, Perkin Elmer, Cambridge, UK) which utilises an argon laser as the illumination beam (488nm). A schematic of the integrated setup is shown in Figure 1. This setup enabled in-plane tracking of the AVIC nuclei during the stress-relaxation and creep tests.

As the fibres in AV tissue are primarily localised in the outer ventricularis and fibrosa layers of the AV, the kinematics of microstructural reorganisation was investigated within both layers during both stress-relaxation and creep tests. For doing so, specimens were secured in the rig in a manner that either the fibrosa or ventricularis side was faced down, depending on the layer under investigation. The initial grip to grip length was set at 10 mm, after which the grip length was adjusted until the specimens straightened and were observed to subtly lift off the cover slip, corresponding to a tare load in the order of magnitude 0.01N, at which point a consistent zero position was defined. The applied strains were calculated based on this adjusted sample length. Hydration of the samples during testing was maintained by immersion in a DMEM bath within the rig. Imaging was carried out in the central region of the specimens (see Figure 1b for a schematic representation), at a depth 50 μm to 80 μm into the designated layer, using a ×20 objective lens (Plan Apo; Nikon, Kingston-Upon-Thames, UK), providing a 670 μm × 500 μm field of view. A typical confocal image of the field of view is shown in Figure 1b. To give an idea of the length-scale at which confocal imaging has been carried out, images of the fibrous microstructure, i.e. collagen fibres and elastin, is also shown in Figure 1b in the same length-scale at which the cell nuclei images are obtained. What we refer to as 'fibres' in this paper are the shown entities at this length-scale.

The movement of the cell nuclei during each hold period of a stress-relaxation or creep test was tracked, obtaining a sequence of confocal microscopy images at a rate of 1 frame per second. Particle tracking software (IMARIS$^{®}$, Bitplane AG) was utilised to determine the (x, y) coordinates of the centroid of each nuclei in each frame, from which the trajectory of movement of each nucleus over the whole stress-relaxation or creep test period was reconstructed, as described in §3. No other data, e.g. force vs time during relaxation or strain vs time during creep tests was recorded.

2.1. Stress-relaxation tests

A total of 120 samples were used for the stress-relaxation tests, half of which were viewed from the ventricularis side and the other half from the fibrosa side. For any test, a sample was taken to a single predefined strain value (ε) at a rate of 60%/min and held for 300s whilst the cell nuclei were imaged, ensuring a loading protocol consistent with our previous tissue-level relaxation study (Anssari-Benam et al. 2011a) and enabling us to

compare the results at both tissue and micro levels. Ten predefined strain levels were used for the course of stress-relaxation tests, ranging from ε = 0% to ε = 20% in increments of 2%, with 3 repeats carried out at each increment.

2.2. Creep tests

For creep tests, a total of 84 samples were utilised. Similar to the stress-relaxation experiments, the samples were divided into two groups, to be viewed from either the ventricularis or the fibrosa sides, each group containing 42 specimens. 7 pre-defined load levels were used, from f = 0 N to f = 3.5 N in increments of 0.5 N. Each sample was loaded to a single force increment at 60%/min and held for 300s, ensuring consistency with our previous tissue-level creep study (Anssari-Benam et al. 2011a), and enabling data comparisons at tissue and microstructure levels. Three samples were tested at each force increment.

3. The kinematics of AV microstructure reorganisation during stress-relaxation and creep tests

From the reconstructed trajectories of movement, it was evident that nuclei moved in either a curvilinear or straight-line manner during both stress-relaxation and creep tests. A method of quantifying the curvilinear and/or straight-line trajectory of each nucleus was therefore established, in order to characterise the relevant kinematics of each nuclei at each strain/force increment.

The radius of curvature r of the curvilinear trajectory pertinent to the curvilinear motion of the cell nuclei was determined for each nucleus by taking the coordinate points (x, y) of the entire reconstructed trajectory of that nucleus, from t = 0s to t = 300s, and fitting these to the equation of a circle (i.e. $(x-a)^2 + (y-b)^2 = r^2$) in MATLAB®. A schematic representation of this procedure is illustrated in Figure 2a. A mean value of r over the hold period was calculated for each sample at each strain/loading increment, by averaging the established r values of all tracked nuclei in the field of view.

It was experimentally observed that as the applied load/strain on the specimens increased, the curvilinear motion of the nuclei gradually gave way to a more straight-line

motion kinematics. This switch between the two kinematics was also reflected in the calculated mean and standard deviation values of the radii of curvature, where a noticeable increase in both values was observed to occur as the strain/load increased. In stress-relaxation tests, the strain increment that appeared to differentiate the curvilinear motion of the nuclei from a straight-line motion was $\varepsilon = 12\%$, while in creep tests this transition was observed to occur at $f = 1.5$ N (see sections 3.1 and 3.2). To document the straight-line motion kinematics, the reconstructed trajectory of each nucleus over the hold period, i.e. at $t = 0$s and $t = 300$s, was fitted to the equation of a line (i.e. $y = ax + b$). Trajectories that resulted in $R^2 \geq 0.98$ were taken as a straight-line path and the associated motion was assumed to be commensurate with straight-line motion kinematics. The displacement of each nucleus was then calculated along its direction of movement. A schematic of this procedure is shown in Figure 2b. A mean value of nuclei displacement over the hold period was then calculated for each sample at each strain/loading increment, by averaging the displacement values of all tracked nuclei in the field of view.

3.1. Stress-relaxation

Typical reconstructed trajectories of nuclei over the 300s stress-relaxation tests are shown in Figure 3, incorporating the fitted circles and straight lines which best described the coordinates of the typical trajectories.

For all applied strain increments in the radial direction, and strains $\varepsilon < 6\%$ in the circumferential direction, the microscopy images showed no detectable movement of the nuclei during relaxation, indicating no detectable microstructural reorganisation. However, for $\varepsilon \geq 6\%$ in the circumferential direction, an evident movement was documented. The nuclei movement at strains $6\% \leq \varepsilon \leq 12\%$ appeared curvilinear (Figure 3a), across both the ventricularis and fibrosa layers. For $\varepsilon > 12\%$, the nuclei movement became increasingly linear in nature across both layers and the reconstructed trajectories predominantly resembled a straight-line motion. Typical straight-line trajectories are presented in Figure 3b along with the best line of fit. The average radii of curvature of the trajectories, and the linear displacements at each respective increment are presented in Figure 3c. The presented values are mean ± SD.

3.2. Creep

Under creep loading, nuclei movement was evident at all loading levels in both the circumferential and radial directions. However, it was not possible to ascertain whether nucleus movement was a direct result of reorganisation of the AV tissue microstructure, or simply due to the fact that the tissue is constantly strained, as a result of which movement of the tissue matrix is to be expected. As stress relaxation tests showed no detectable structural reorganisation in the radial direction, we adopt caution in our analysis and focus the creep kinematics analysis only on the datasets obtained from the circumferential direction. While some of the observed kinematics in circumferential creep tests will also likely relate to the continuous straining of the tissue, results should also reflect, at least in part, the kinematics occurring as a result of the AV microstructural reorganisation.

During the circumferential creep tests, AVIC nuclei demonstrated curvilinear and straight-line patterns of motion in both the ventricularis and fibrosa layers, similar to the kinematic modes observed during stress-relaxation tests. Typical reconstructed trajectories are presented in Figure 4. Results indicate that at lower levels of load ($\leq 1.5N$), the dominant kinematics is curvilinear movement (Figure 4a). With increased applied load, the curvilinear motion gradually switches to linear displacement kinematics (Figure 4b). The average radii of curvature and the linear displacements of the nuclei in their trajectories are presented in Figure 4c (mean $\pm$ SD).

3.3. Summary of the experimental observations

If perfect attachment of the AVICs to the fibres is assumed, from these results one may characterise the kinematics of the fibre reorganisation within the AV tissue during the stress-relaxation and creep phenomena as follows:

(i) At lower strains and loads, pronounced curvilinear kinematics of the fibres are evident, suggesting that when the fibres are likely wavy, fibre rotation is the dominant mode; and

(ii) At higher strains and loads, where the fibres are likely straight and recruited, linear motion is the dominant mode of kinematics.

The above kinematics were consistent in both the ventricularis and fibrosa layers.

4. How these kinematics result in stress-relaxation and creep modes

We will now show analytically how this microstructural reorganisation during stress-relaxation or creep may lead to the respective well-known exponential decay of stress, or primary and secondary creep strains, at the tissue level. We will seek to mathematically formulate the observed fibre kinematics and derive the ensuing relaxation and creep behaviours accordingly. The theoretical criterion and the notations used here are based on those postulated by Mijailovich et al. (1993) and Kojic et al (1998), adapted here to be more readily applicable to a collagenous tissue such as the AV with the following idealised description of its structure.

4.1. An idealised structural description of the AV microstructure

The three main structural constituents of the AV may be considered as the collagen fibres, elastin network and the hydrophilic GAGs. Collagen fibres are packed into *bundles* which principally align along the circumferential direction (see, e.g., Rock et al. 2014), visible at the macro-level. These bundles are embedded within a *ground matrix* predominantly composed of the elastin network and GAGs. The elastin network is thought to be principally responsible for the elastic recoil of the AV, and not associated with viscoelastic attributes. The dissipative kinematics of fibre-fibre and fibre-matrix interactions are therefore attributed to the microstructural reorganisation of the collagen fibres within the GAG-rich matrix, upon the application of tissue-level deformations (see, e.g., Anssari-Benam et al. 2016). The fibres are primarily crimped in the unstrained state. As the tissue is strained, the fibres gradually straighten and re-orientate towards the loading direction; a process known as fibre recruitment. When fully straight and recruited, the fibres will then become strained. With these considerations, in the following we first establish the relationships governing the kinematics of straight fibres, followed by those governing the curvilinear kinematics pertaining to wavy fibres.

4.2. Fibre kinematics framework for straight fibres

We begin our analysis of fibre kinematics under time-dependent deformation by considering two recruited (i.e. straight and aligned) adjacent fibres of length *l*, as shown schematically in Figure 5.

Upon the application of an external load on the tissue, **F_external**, let us assume that the arbitrary pair of adjacent straight fibres 1 & 2 in Figure 5 will be subjected to tensile forces F_1 and F_2, respectively, at opposite ends to each other. Note that **F_external** is a generic load, arising from either uniaxial or biaxial tissue-level loading. Irrespective of loading modality, F_1 and F_2 will always be axial, i.e. along the axis of the fibres.

In general, the contact force between the two fibres may possess two components: (i) a normal component to the surface of each fibre denoted here as N; and (ii) a tangential component to the surface of each fibre denoted here as T. Physically, N may represent the transverse mechanical loads (e.g. Poisson ratio effects), as well as any other microenviroment originated loading; and T may be interpreted as the frictional force between the two fibres. The exact nature of contact between two adjacent fibres in the AV tissue remains poorly understood, as with most collagenous soft tissues (Mijailovich et al. 1993). However, it may be assumed that there are regions along the fibres where there is direct contact between the two fibres, interspersed with regions where fibres are separated from each other by a thin layer of ground substance, wherein the fibres are embedded (Kojic et al. 1998).

Therefore, over a length dx of the fibres, shown in Figure 5, the tangential traction force T between the fibres may be presented as:

$$T(x,t) = \pm\mu N(x) + C_d V_{rel}(x,t) \tag{1}$$

Here, the term $\mu N(x)$ represents the classic Coulomb friction force, and $C_d V_{rel}(x,t)$ is the Newtonian viscous force (analogous to viscous force in a damper). C_d would therefore assume the role of the viscous damping coefficient of the ground substance, and $V_{rel}(x,t)$ is the relative velocity of the fibres sliding against each other. Assuming that fibres behave linearly elastic when fully straight (e.g. Sacks 2003), the traction force $T(x,t)$ may be derived as (see appendix A for the details of the derivation and the incorporated assumptions):

$$T(x,t) = C_d \frac{\partial}{\partial t}\big(u_1(x,t) - u_2(x,t)\big) \tag{2}$$

Note that we have replaced the relative velocity $V_{rel}(x,t)$ with its partial differential form $\frac{\partial}{\partial t}\big(u_1(x,t) - u_2(x,t)\big)$, i.e. the partial differential of the relative displacement of the material

11

points in two fibres $(u_1(x,t) - u_2(x,t))$ with respect to time t. Substituting equation (2) into (A.6):

$$AE \frac{\partial^2}{\partial x^2}(u_1(x,t) - u_2(x,t)) = 2C_d \frac{\partial}{\partial t}(u_1(x,t) - u_2(x,t)) \tag{3}$$

By summing equations $(A.5)_1$ and $(A.5)_2$:

$$\frac{\partial^2(u_1(x,t) + u_2(x,t))}{\partial x^2} = 0 \tag{4}$$

Therefore:

$$\frac{\partial}{\partial x}\left(\frac{\partial(u_1(x,t) + u_2(x,t))}{\partial x}\right) = 0 \Rightarrow \frac{\partial(u_1(x,t) + u_2(x,t))}{\partial x} = C_1 + f_1(t) \tag{5}$$

where C_1 is a constant and $f_1(t)$ is a function of time. However, in light of equations (A.2) and (A.3), and the assumption of the geometrical and mechanical uniformity of the fibres, one may establish that $C_1 = 0$, and $f_1(t) = \dfrac{F(t)}{AE}$. Note that A and E are the cross-sectional area and the elastic modulus of the fibre, respectively. Substituting for these two terms into equation (5) and performing integration over x yields:

$$u_1(x,t) + u_2(x,t) = \frac{F(t)}{AE}x + f_2(t) + C_2 \tag{6}$$

where C_2 is a constant and $f_2(t)$ is a function of time. We note, however, since at $x = 0$ we must have $u_1(0,t) = -u_2(0,t)$, C_2 and $f_2(t)$ must both assume 0. Therefore, the following relationship may be obtained:

$$u_2(x,t) = \frac{F(t)}{AE}x - u_1(x,t) \tag{7}$$

Substituting equation (7) into (3) one gets:

$$AE \frac{\partial^2}{\partial x^2}u_1(x,t) = 2C_d \frac{\partial}{\partial t}\left(u_1(x,t) - \frac{F(t)}{2AE}x\right) \tag{8}$$

Equation (8) represents the fibre kinematics based on fibre-fibre and fibre-matrix interactions. In order to achieve an exact analytical solution for the particular time-dependent behaviour of interest, i.e. stress-relaxation or creep, appropriate boundary conditions supported by the kinematics of fibres must be sought and implemented. In this regard, by assuming that the adjacent fibres strain such that there is no relative movement

between the fibres at their centres (where $x = 0$), i.e. $\frac{\partial u_{rel}(0,t)}{\partial x} = 0$, it follows that:

$\frac{\partial u_1(0,t)}{\partial x} = \frac{\partial u_2(0,t)}{\partial x}$. In light of equations (A.2) and (A.3), it may be deduced that

$F(t) = F_1(x,t) + F_2(x,t) = AE \frac{\partial}{\partial x}\big(u_1(x,t) + u_2(x,t)\big)$, and therefore:

$$\frac{\partial u_1(0,t)}{\partial x} = \frac{F(t)}{2AE} \tag{9}$$

The expression in equation (9) provides one boundary condition for equation (8). We shall introduce additional boundary conditions as appropriate when solving for stress-relaxation or creep behaviours in the following sections, in accordance with the mechanics of each phenomenon and the relevant fibre kinematics.

4.3. Fibre kinematics framework for wavy fibres

At lower strains/loads (e.g. $6\% \leq \varepsilon \leq 12\%$ or $f \leq 1.5\,\text{N}$), where fibres are still likely wavy and not likely yet fully recruited, the dominant kinematics of AV microstructural reorganisation during stress-relaxation and creep was observed to be curvilinear, suggesting fibre rotation, as demonstrated in §3. To this end, consider two adjacent wavy fibres at t = 0s, embedded within the surrounding matrix as schematised in Figure 6. As a result of the structural reorganisation during stress-relaxation or creep, the fibres may rotate by an arbitrary amount and change their length, to arrive at their final configuration at $t = 300\text{s}$ as shown in the figure. From the theory of 2D elasticity for uniaxial plane stress in this composite mixture:

$$\sigma_x = \frac{E_c}{1-\upsilon_c^2}\left[\frac{\partial u}{\partial x} + \upsilon_c \frac{\partial u}{\partial y}\right] \tag{10}$$

where σ_x is the principal stress along direction x, and E_c and υ_c are the overall elastic and Poisson ratio moduli of the composite, respectively. Using this criteria and under the assumption of incompressibility for the matrix, the governing fibre kinematics equation for a wavy fibre as the counterpart to equation (8) can be derived as (see Appendix B for the details):

$$\frac{\phi AE}{(1-\upsilon^2)}\frac{\partial^2}{\partial x^2}u_1(x,t) = 2C_d \frac{\partial}{\partial t}\left(u_1(x,t) - \frac{(1-\upsilon^2)F(t)}{2\phi AE}x\right) \tag{11}$$

13

where ϕ is a parameter between $0 < \phi < 1$, $\upsilon = \upsilon_c \to 0.5$, and A and E are the cross-sectional area and the elastic modulus of the fibre, respectively, as per the previous case. Accordingly, adopting the similar boundary condition of no relative movement of fibres at their centres given in equation (9):

$$\frac{\partial u_1(0,t)}{\partial x} = \frac{(1-\upsilon^2)F(t)}{\phi\,AE} \tag{12}$$

Additional appropriate boundary conditions will again be introduced in the following sections in order to obtain specific solutions for stress-relaxation and creep functions, accordingly.

4.4. Exponential-decay stress-relaxation

Using the derived governing fibre kinematics equations, we now aim to show how the experimentally observed fibre reorganisation can give rise to exponential stress-relaxation as seen in tissue level experiments. Let us again start with the case of straight fibres. For this case, in addition to the boundary condition ascribed by equation (9), another boundary condition for stress relaxation is established by noting that:

$$u_1(\frac{l}{2},t) = \frac{l}{2AE}\,F(0) \tag{13}$$

where within the context of stress-relaxation, $F(0)$ is the initial force acting on the fibre at $t = 0$, i.e. at the start of the relaxation process. This condition ensures that the displacement of the fibre, at the loaded end, remains constant over time, as required in stress relaxation. With boundary conditions (9) and (13), we can now solve the fibre-kinematics equation (8) for straight fibres. Using the change of variables: $v(x,t) = u_1(x,t) - \dfrac{F(t)}{2AE}x$, equation (8) may be re-written as:

$$\frac{AE}{2C_d}\frac{\partial^2 v(x,t)}{\partial x^2} = \frac{\partial v(x,t)}{\partial t} \tag{14}$$

The new boundary conditions will therefore be described by:

$$\frac{\partial v(0,t)}{\partial x} = 0 \quad , \quad \frac{\partial v(\frac{l}{2},t)}{\partial x} = \frac{F(t)}{2AE}, \quad v_1(\frac{l}{2},t) = \frac{l}{2AE}(F(0) - \frac{F(t)}{2}) \tag{15}$$

This change of variable renders equation (14) and the boundary conditions in (15) reminiscent of a specialised case of the heat transfer equation in a slab heated by radiation with a constant initial temperature, as advocated by Mijailovic et al. (1993). An analytical solution for this equation is presented by Carslaw and Jaeger (1959), and by substituting $u(x,t)$ for $v(x,t)$, the solution to equation (8) may be obtained as:

$$u_1(x,t) = \frac{F(t)}{2AE}x + \frac{l\,F(0)}{2AE}\left[1 - \sum_{n=1}^{\infty} \frac{2\cos\left(\frac{2\gamma_n x}{l}\right)\sec\gamma_n}{2 + \gamma_n^2}\exp\left(-(\frac{\gamma_n^2 AE}{2C_d l^2})t\right)\right] \qquad (16)$$

where γ_n are positive roots of $\gamma_n \tan\gamma_n = 1$ (Carslaw and Jaeger 1959).

Substituting equation (16) into (A.3), for the fibre loaded end at $x = l/2$, gives the relaxation force as:

$$F(t) = F_0 \sum_{n=1}^{\infty} \frac{4}{2 + \gamma_n^2}\exp\left(-(\frac{\gamma_n^2 AE}{2C_d l^2})t\right) \qquad (17)$$

Similarly for the case of wavy fibre, in order to solve equation (11) for stress relaxation, another boundary condition in addition to (12) is required and may be established by:

$$u_1(\frac{l}{2},t) = \frac{l(1-\upsilon^2)}{2\phi AE}F(0) \qquad (18)$$

where again $F(0)$ is the initial force at $t = 0$, i.e. at the start of the relaxation process, acting on the fibre. We shall also use the following change of variables: $v(x,t) = u_1(x,t) - \frac{(1-\upsilon^2)F(t)}{2\phi AE}x$, to re-write equation (11) as:

$$\frac{\phi\,AE}{2C_d(1-\upsilon^2)}\frac{\partial^2 v(x,t)}{\partial x^2} = \frac{\partial v(x,t)}{\partial t} \qquad (19)$$

with the new boundary conditions as:

$$\frac{\partial v(0,t)}{\partial x} = 0 \ , \quad \frac{\partial v(\frac{l}{2},t)}{\partial x} = \frac{(1-\upsilon^2)F(t)}{2\phi AE} \ , \quad v_1(\frac{l}{2},t) = \frac{l(1-\upsilon^2)}{2\phi AE}(F(0) - \frac{F(t)}{2}) \qquad (20)$$

Therefore, the solution to equation (11) can now be obtained as:

$$u_1(x,t) = \frac{(1-\upsilon^2)F(t)}{2\phi AE}x + \frac{l\,(1-\upsilon^2)F(0)}{2\phi AE}\left[1 - \sum_{n=1}^{\infty}\frac{2\cos\left(\dfrac{2\gamma_n x}{l}\right)\sec\gamma_n}{2+\gamma_n^2}\exp\left(-(\frac{\gamma_n^2\,\phi\,AE}{2C_d(1-\upsilon^2)l^2})t\right)\right]$$

(21)

where again γ_n are positive roots of $\gamma_n\tan\gamma_n = 1$ (Carslaw and Jaeger 1959). Substituting equation (21) into (B.2), for the loaded end at $x = l/2$, gives the relaxation force as:

$$F(t) = F_0\sum_{n=1}^{\infty}\frac{4}{2+\gamma_n^2}\exp\left(-(\frac{\gamma_n^2\,\phi\,AE}{2C_d(1-\upsilon^2)l^2})t\right)$$

(22)

Therefore, the relaxation force due to the kinematics of the reorganisation of the fibre population within the tissue during stress relaxation can be summarised as:

$$\begin{cases} F(t) = F_0\sum_{n=1}^{\infty}\dfrac{4}{2+\gamma_n^2}\exp\left(-(\dfrac{\gamma_n^2\,\phi\,AE}{2C_d(1-\upsilon^2)l^2})t\right) \\[4pt] (\textit{at lower strains where fibre rotation may be dominant}) \\[12pt] F(t) = F_0\sum_{n=1}^{\infty}\dfrac{4}{2+\gamma_n^2}\exp\left(-(\dfrac{\gamma_n^2 AE}{2C_d l^2})t\right) \\[4pt] (\textit{at higher strains where fibre sliding may be dominant}) \end{cases}$$

(23)

Alternatively, dividing both sides of the above equations by fibre area A, one gets the equivalent following terms as functions of stress:

$$\begin{cases} \sigma(t) = \sigma_0\sum_{n=1}^{\infty}\dfrac{4}{2+\gamma_n^2}\exp\left(-(\dfrac{\gamma_n^2\,\phi\,AE}{2C_d(1-\upsilon^2)l^2})t\right) \\[4pt] (\textit{at lower strains where fibre rotation may be dominant}) \\[12pt] \sigma(t) = \sigma_0\sum_{n=1}^{\infty}\dfrac{4}{2+\gamma_n^2}\exp\left(-(\dfrac{\gamma_n^2 AE}{2C_d l^2})t\right) \\[4pt] (\textit{at higher strains where fibre sliding may be dominant}) \end{cases}$$

(24)

where $\sigma(t)$ is the stress at time t, and σ_0 is the initial stress at $t = 0$, i.e. at the start of the relaxation process, acting on the fibre.

These equations underline that fibre-fibre and fibre-matrix interactions, which occur as a result of the structural reorganisation of the collagen fibre population during the relaxation

process, will result in an exponential decay of stress. This result is consistent with the observation in stress-relaxation experiments. These analyses strongly suggest that exponential relaxation of stress in planar collagenous tissues such as the AV may be explained at the tissue micro-structure level, based on the kinematics of collagen fibre rotation and sliding.

4.5. Primary and secondary creep

Equation (8) describes the governing equation of fibre kinematics for a straight fibre. To solve this equation for creep, a boundary condition is established by noting that:

$$\frac{\partial u_1(\frac{l}{2}, t)}{\partial x} = \frac{F(0)}{AE} \tag{25}$$

This boundary condition ensures that the force at the loaded end of the fibre remains constant over time t, as required during creep behaviour. Note that $F(0)$ is the initial force at $t = 0$, i.e. at the start of the creep process, acting on the fibre.

Using the prescribed change of variable in §4.3, equation (8) may be solved for creep to obtain the following function (Carslaw and Jaeger 1959):

$$u_1(x, t) = \frac{F(0)}{2l\,C_d}t + \frac{l\,F(0)}{2AE}\left[\frac{12x^2 - l^2}{6l^2} - \frac{2}{\pi^2}\sum_{n=1}^{\infty}\frac{(-1)^n}{n^2}\exp\left(-(\frac{n^2\pi^2 AE}{2C_d l^2})t\right)\cos\frac{2n\pi x}{l}\right] \tag{26}$$

It follows that displacement at the fibre loaded end $x = l/2$, denoted henceforth by $U(t)$, will be:

$$U(t) = \frac{F(0)}{2l\,C_d}t + \frac{l\,F(0)}{2AE}\left[\frac{1}{3} - \frac{2}{\pi^2}\sum_{n=1}^{\infty}\frac{1}{n^2}\exp\left(-(\frac{n^2\pi^2 AE}{2C_d l^2})t\right)\right] \tag{27}$$

Similarly, for the case of wavy fibre, equation (11) may be solved for creep by utilising the change of variable described in §4.3, and noting that $\dfrac{\partial u_1(\frac{l}{2}, t)}{\partial x} = \dfrac{(1 - \upsilon^2)}{\phi\,AE}F(0)$, to obtain:

$$u_1(x,t) = \frac{(1-\upsilon^2)F(0)}{2\,l\,C_d}t + \frac{l\,(1-\upsilon^2)\,F(0)}{2\phi AE}\left[\frac{12x^2-l^2}{6l^2} - \frac{2}{\pi^2}\sum_{n=1}^{\infty}\frac{(-1)^n}{n^2}\exp\left(-(\frac{n^2\pi^2\phi\,AE}{2C_d l^2(1-\upsilon^2)})t\right)\cos\frac{2n\pi x}{l}\right]$$

(28)

and therefore the displacement at the fibre loaded end will be:

$$U(t) = \frac{(1-\upsilon^2)F(0)}{2\,l\,C_d}t + \frac{l\,(1-\upsilon^2)\,F(0)}{2\phi AE}\left[\frac{1}{3} - \frac{2}{\pi^2}\sum_{n=1}^{\infty}\frac{1}{n^2}\exp\left(-(\frac{n^2\pi^2\phi\,AE}{2C_d l^2(1-\upsilon^2)})t\right)\right]$$ (29)

Equations (27) and (29) describe the displacement of the fibre at the loaded end during creep. Alternatively, by dividing both sides of the two equations by fibre length l, one may obtain the following terms as functions of strain:

$$\begin{cases}\varepsilon(t) = \frac{(1-\upsilon^2)F(0)}{2\,l^2\,C_d}t + \frac{(1-\upsilon^2)\,F(0)}{2\phi AE}\left[\frac{1}{3} - \frac{2}{\pi^2}\sum_{n=1}^{\infty}\frac{1}{n^2}\exp\left(-(\frac{n^2\pi^2\phi\,AE}{2C_d l^2(1-\upsilon^2)})t\right)\right] \\ (at\ lower\ strains\ where\ fibre\ rotation\ may\ be\ dominant) \\[2mm] \varepsilon(t) = \frac{F(0)}{2\,l^2\,C_d}t + \frac{F(0)}{2AE}\left[\frac{1}{3} - \frac{2}{\pi^2}\sum_{n=1}^{\infty}\frac{1}{n^2}\exp\left(-(\frac{n^2\pi^2 AE}{2C_d l^2})t\right)\right] \\ (at\ higher\ strains\ where\ fibre\ sliding\ may\ be\ dominant)\end{cases}$$

(30)

These equations highlight that the creep behaviour of collagenous soft tissues such as the AV may stem from the same dissipative kinematics that give rise to stress-relaxation, only with different boundary conditions pertinent to each behaviour. In other words, AV stress-relaxation and creep phenomena at the microstructural level appear to be coupled, stemming from the same mechanism(s) and mathematically interrelated.

5. Correlation with the tissue-level behaviour

Our previous study documented the stress-relaxation and creep behaviours of AV specimens under uniaxial loading (Anssari-Benam et al. 2011a). It was established that AV relaxation behaviour exhibited a single exponential decay mode at all tested strain levels in the radial direction, as well as at lower strain levels ($\varepsilon < 6\%$) in the circumferential direction. At higher circumferential strains ($\varepsilon \geq 6\%$), relaxation was characterised by double exponential decay modes (Anssari-Benam et al. 2011a). For the case of creep, an exponential primary creep followed by a linear secondary creep behaviour was observed at

almost all loading levels in both directions (Anssari-Benam et al. 2011a). The current experimental results highlighted no detectable fibre reorganisation/movement during stress-relaxation in the radial direction at any strain levels, nor in the circumferential direction at strains $\varepsilon < 6\%$. However, at strain levels $6\% \leq \varepsilon \leq 12\%$, curvilinear motion was the dominant kinematics, and at higher strains ($\varepsilon > 12\%$) the dominant kinematics switches to linear sliding. In creep, curvilinear motion was dominant at loading levels $f \leq 1.5\,\text{N}$, and linear displacement at $f > 1.5\,\text{N}$. Table 1 summarises these results for a quick comparison.

In the following sections we aim to show how stress-relaxation and creep functions in equations (24) and (30), derived from the observed fibre kinematics in §3, is correlated with the tissue-level behaviour summarised in Table 1.

5.1. Stress-relaxation modes

For strains $\varepsilon < 6\%$, a single exponential decay mode was observed at the tissue level (Anssari-Benam et al. 2011a), while no notable fibre kinematics was detected. Therefore, this dissipation of stress is not likely to have been caused by the dissipative effects of fibre rotation/sliding. It is thus strongly likely that this dissipation stems from the non-fibrous GAGs and water content of the tissue. The viscous fluid-like behaviour of proteoglycans and proteoglycan/water mixtures have been well established and documented through the celebrated works of Van C. Mow (e.g. see Mow et al. 1984 and Zhu et al. 1996) amongst others, and shear-thinning behaviour of the AV tissue has been attributed to the viscous characteristics of the GAGs (Anssari-Benam et al. 2011b; 2016; 2017). We therefore postulate that the exponential decay of stress at low strains is facilitated by the viscous flow-like behaviour of the GAGs/water mixture within the AV tissue as a result of the tissue-level deformation, similar to a *Maxwell* viscous flow.

For strains $\varepsilon > 6\%$, AV tissue exhibits two relaxation modes (Anssari-Benam et al. 2011a). As described above, one relaxation mode likely stems from the viscous flow-like behaviour of the GAGs/water content. However, we note that for $6\% \leq \varepsilon \leq 12\%$ and $\varepsilon > 12\%$, where the fibre kinematics are predominantly curvilinear and linear movement respectively, stress $\sigma(t)$ decays with time t according to equation (24). If one inspects the

$\sum\limits_{i=1}^{n}$ terms in that equation more closely, it is evident that the numerical values of those terms would be much smaller for $n \geq 2$ compared to that for $n = 1$ (by orders of magnitude depending on the values of the parameters inside the argument of the exponential function), rendering those terms numerically insignificant. Thus, the stress-relaxation relationships in equation (24) can be simplified with a good degree of accuracy to:

$$
\begin{cases}
\sigma(t) = \dfrac{4\,\sigma_0}{2+\gamma_1^2}\exp\left(-(\dfrac{\gamma_1^2\phi\,AE}{2C_d(1-\upsilon^2)l^2})t\right) & , \quad \text{in rotation} \\[4mm]
\sigma(t) = \dfrac{4\,\sigma_0}{2+\gamma_1^2}\exp\left(-(\dfrac{\gamma_1^2\,AE}{2C_d l^2})t\right) & , \quad \text{in linear sliding}
\end{cases}
\tag{31}
$$

Thus, the dissipative effects of fibre kinematics during stress-relaxation, in the form of either fibre reorientation or fibre sliding, facilitate another mode of stress decay through the exponential terms presented in equation (31). We note that these decay modes correspond to the '*slow*' relaxation mode of the tissue level AV stress-relaxation, while the viscous flow-like behaviour of the GAGs/water content would account for the '*fast*' relaxation mode.

5.2. Creep modes

In §5.1 we postulated that GAGs/water mixture behaved as a *Maxwell* viscous fluid, and thus give rise to one of the exponential relaxation modes. A *Maxwell* fluid is not capable of exhibiting (primary) creep, therefore one may conclude that the observed exponential primary and linear secondary creep at the tissue level stem from the kinematics shown in §3.2, and formulated by equation (30).

Similar to the stress-relaxation equations, by inspecting equation (30) for creep more closely, the $\sum\limits_{i=1}^{n}$ terms are negligible for $n \geq 2$ compared to that for $n = 1$, consequently rendering those terms numerically insignificant. In light of this analysis, one may re-write the relationships given in equation (30) with a good level of accuracy as:

$$\begin{cases} \varepsilon(t) = \dfrac{(1-\upsilon^2)F(0)}{2\,l^2\,C_d}t + \dfrac{(1-\upsilon^2)\,F(0)}{2\phi AE}\left[\dfrac{1}{3} - \dfrac{2}{\pi^2}\exp\left(-(\dfrac{\pi^2\phi\,AE}{2C_d l^2(1-\upsilon^2)})t\right)\right] & \text{, in rotation} \\[4mm] \varepsilon(t) = \dfrac{F(0)}{2\,l^2\,C_d}t + \dfrac{F(0)}{2AE}\left[\dfrac{1}{3} - \dfrac{2}{\pi^2}\exp\left(-(\dfrac{\pi^2 AE}{2C_d l^2})t\right)\right] & \text{, in linear sliding} \end{cases} \quad (32)$$

Equation $(32)_1$ describes the creep behaviour in lower strains (e.g. corresponding to $f \le 1.5\,\mathrm{N}$) where the fibre reorientation may be the dominant kinematics, and equation $(32)_2$ describes the creep behaviour at higher strains where fibre sliding is more dominant.

The set of equations in (32) highlights the origin of AV primary and secondary creep modes. At shorter time periods, the exponential term in (32) dominates the trend of variation in $\varepsilon(t)$, resulting in tissue-level primary creep. At longer time periods, the exponential effect abates, because the numerical value of the exponential function decreases as time elapses. The $\varepsilon(t)$ creep function is then influenced by the linear term in t, resulting in tissue-level secondary creep.

5.3. Creep behaviour in uniaxial versus biaxial loading

The mathematical framework presented in §4 clearly demonstrates that the governing fibre-kinematic equation for both stress-relaxation and creep behaviours is the same, but only the loading boundary conditions is different, which mathematically results in either the stress-relaxation (equation (24)) or creep function (equation (30)), depending on the applied loading boundary condition. The predicted stress-relaxation and creep functions were shown to correlate well with the tissue-level experimental data in §§5.1 and 5.2. One conclusion from this analysis is that the loading boundary condition clearly plays an important role in tissue-level response. This notion can be extended to explain why creep behaviour in uniaxial loading is different to that under equi-biaxial loading when tested on the AV tissue. Under equi-biaxial loading conditions, Stella et al. 2007 have reported minimal creep response, much lower than that observed under uniaxial loading.

Exhibiting lower levels of creep under equi-biaxial loading is not specific to the AV tissue. Indeed, it is a common and established feature of many materials, having been also shown in tissues such as the ligament (Tan et al. 2016) as well as polymeric materials (see,

e.g., Nielsen and Landel 1994). Equi-biaxial loading condition is such that it tends to preserve the microstructural arrangement of the subject sample more so than other in-plane loading conditions (e.g. see Alavi et al. 2013 for a comparative study on bovine pericardial leaflets). Thus, equi-biaxial loading boundary condition facilitates much less microstructural reorganisation, and therefore less dissipative kinematics will ensue. In addition to this experimental observation, it is also possible to mathematically show why creep under equi-biaxial loading would be lower than uniaxial creep *a priori*.

In order to make the analysis relevant to the AV, let us consider a transversely isotopic Kelvin-Voigt viscoelastic material. We choose a Kelvin-Voigt material as it is the simplest viscoelastic unit capable of exhibiting creep, and we choose 'transverse isotropy' to reflect the material symmetry characteristics of the AV tissue. The generalised 3D constitutive relationships between stress, strain and time for such a material with fibres primarily aligned along the *x* direction in *x*-*y* plane has been derived and presented in Appendix C as:

$$
\begin{cases}
\varepsilon_x(t) = \dfrac{\sigma_x(t)}{E_x} - \upsilon_{yx}\dfrac{\sigma_y(t)}{E_y} - \upsilon_{zx}\dfrac{\sigma_z(t)}{E_z} - \dfrac{\eta\,\upsilon_{xy}}{E_x\,\upsilon_{yx}}\left[A\dot{\varepsilon}_x(t)\right] \\[4mm]
\varepsilon_y(t) = \dfrac{\sigma_y(t)}{E_y} - \upsilon_{xy}\dfrac{\sigma_x(t)}{E_x} - \upsilon_{zy}\dfrac{\sigma_z(t)}{E_z} - \dfrac{\eta}{E_y}\left[B\dot{\varepsilon}_y(t)\right] \\[4mm]
\varepsilon_z(t) = \dfrac{\sigma_z(t)}{E_z} - \upsilon_{xz}\dfrac{\sigma_x(t)}{E_x} - \upsilon_{yz}\dfrac{\sigma_y(t)}{E_y} - \dfrac{\eta}{E_z}\left[C\dot{\varepsilon}_z(t)\right]
\end{cases}
\tag{33}
$$

which for a planar thin membrane tissue such as the AV may be simplified to:

$$
\begin{cases}
\varepsilon_x(t) = \dfrac{\sigma_x(t)}{E_x} - \upsilon_{yx}\dfrac{\sigma_y(t)}{E_y} - \dfrac{\eta\,\upsilon_{xy}}{E_x\,\upsilon_{yx}}\left[A\dot{\varepsilon}_x(t)\right] \\[4mm]
\varepsilon_y(t) = \dfrac{\sigma_y(t)}{E_y} - \upsilon_{xy}\dfrac{\sigma_x(t)}{E_x} - \dfrac{\eta}{E_y}\left[B\dot{\varepsilon}_y(t)\right]
\end{cases}
\tag{34}
$$

Under equi-biaxial creep loading conditions, we note that the stress is kept constant at an equal level in both directions from time $t = 0$. Using equation $(34)_1$:

$$
\varepsilon_x(t) + A\frac{\eta\,\upsilon_{xy}}{E_x\,\upsilon_{yx}}\dot{\varepsilon}_x(t) = \sigma_x(0)\left(\frac{1}{E_x} - \frac{\upsilon_{yx}}{E_y}\right)
\tag{35}
$$

Noting that for a transversely isotropic material: $\dfrac{\upsilon_{xy}}{E_x} = \dfrac{\upsilon_{yx}}{E_y}$, equation (35) may be rewritten as:

$$\varepsilon_x(t) + A \frac{\eta\,\upsilon_{xy}}{E_x\,\upsilon_{yx}} \dot{\varepsilon}_x(t) = \frac{\sigma_x(0)}{E_x}\left(1 - \upsilon_{xy}\right) \tag{36}$$

Solving equation (36) under the boundary condition that the strain at $t = 0$ is $\varepsilon_x(0)$ gives the creep strain function in the x direction, namely the circumferential direction of the AV tissue, under equi-biaxial loading as:

$$\varepsilon_x^{equi-biaxial}(t) = \left[\varepsilon_x(0) - \frac{\sigma_x(0)}{E_x}\left(1 - \upsilon_{xy}\right)\right]\exp\left(-\frac{E_x\,\upsilon_{yx}}{A\eta\,\upsilon_{xy}}t\right) + \frac{\sigma_x(0)}{E_x}\left(1 - \upsilon_{xy}\right) \tag{37}$$

and similarly for the radial direction:

$$\varepsilon_y^{equi-biaxial}(t) = \left[\varepsilon_y(0) - \frac{\sigma_y(0)}{E_y}\left(1 - \upsilon_{yx}\right)\right]\exp\left(-\frac{E_y}{B\eta}t\right) + \frac{\sigma_y(0)}{E_y}\left(1 - \upsilon_{yx}\right) \tag{38}$$

Comparatively, under only uniaxial creep testing, the governing differential equation will be $\dfrac{\eta}{E}\dot{\varepsilon}(t) + \varepsilon(t) = \dfrac{1}{E}\sigma(0)$, which is solved for creep strain as:

$$\varepsilon^{uniaxial}(t) = \left[\varepsilon(0) - \frac{\sigma(0)}{E}\right]\exp\left(-\frac{E\,t}{\eta}\right) + \frac{\sigma(0)}{E} \tag{39}$$

Plots in Figure 7 compare the typical equi-biaxial versus the uniaxial creep behaviours using functions in equations (37) to (39). For producing the plots, the numerical data on the initial stress and the corresponding strains were collated from Stella et al. (2007), reporting values of approximately $\sigma_x(0) = \sigma_y(0) = 240$ kPa, $\varepsilon_x(0) = 15\%$ and $\varepsilon_y(0) = 70\%$. To enforce the condition of incompressibility, υ_{xy} was assumed to be $\upsilon_{xy} = 0.5$, while E_x and E_y were chosen to be 0.7 MPa and 0.3 MPa, respectively, for a reasonable representation of the tissue moduli in circumferential and radial directions. A direct comparison between uniaxial and equi-biaxial creep behaviours using those values is shown in Figure 7.

These plots graphically illustrate two important points, that may also be inferred mathamtically from equations (37) to (39): (i) inherently, viscoelastic materials under equi-biaixal loading exhibit lower creep than when loaded uniaxially; and (ii) uniaxial creep

occurs much faster than biaxial creep. Indeed, for a material with low $\frac{\upsilon_{yx}}{\upsilon_{xy}}$ and $\frac{E_x}{\eta}$ ratios, mathematically the biaxial creep may be deemed negligible compared to the uniaxial creep. We note that collagenous soft tissues such as the AV have non-linear mechanical behaviours, where the Poisson ratios may also be a function of time, and therefore a linear Kelvin-Voigt model may introduce approximations and simplifications to the analysis. Notwithstanding those approximations, for a transversely isotropic material such as the AV tissue with typically low $\frac{E_x}{\eta}$ and $\frac{\upsilon_{yx}}{\upsilon_{xy}}$ ratios, the above analysis may suffice to show that the reduced levels of creep under equi-biaxial loading is simply a direct consequence of the loading boundary conditions under biaxial deformation, physically inhibiting the capacity of the samples to exhibit notable levels of creep.

6. Concluding remarks

This study aimed to investigate the microstructural mechanisms that facilitate AV tissue level stress-relaxation and creep behaviours. We investigated the reorganisation of the AV microstructure during both phenomena experimentally, and then underpinned the experimental results by a kinematics framework to account for the dissipative effects of fibre sliding that arise from fibre rotation and linear displacement within the tissue matrix. Our analysis strongly suggests that: (i) the dissipative fibre-fibre and fibre-matrix kinematics due to fibre rotation and linear displacement (i.e. microstructural reorganisation) govern both the relaxation and creep phenomena; (ii) the underlying mechanisms that facilitate both stress-relaxation and creep behaviours are therefore essentially coupled and uniform; and (iii) these mechanisms may be explained at tissue fibre (micro-) level. Further, the mathematical framework presented in this study offers an analytical explanation as to why AV relaxation modes are exponential, and why the tissue exhibits exponential primary creep followed by linear secondary creep. The presented framework therefore provides a mathematical underpinning of the micromechanics of stress-relaxation and creep in the aortic valve. This framework facilitates future development of microstructurally-based models that can predict tissue-level relaxation or creep behaviours based on the microstructural attributes and kinematics.

6.1. Study boundaries and limitations

The experimental methodology utilised in this study has inherent limitations. First, the field of view only covers an area of 670μm × 500μm, compared with the dimensions of strip specimens (5mm × 10mm). However, we also note that it is a common practice in the field of continuum-mechanics to consider a representative volume element (RVE) of the material, and to assume that the entire material possess the same characteristics. Therefore, assuming that fibre kinematics observed within the field of view is a representative of the type and trend of fibre kinematics across the whole sample may be deemed an inevitable approximation.

The loading modality employed in this study was uniaxial; while biaxial loading may represent the physiological loading condition of the AV tissue more closely. Additionally, implicit to our conferred analysis regarding the kinematics of fibres is the assumption of perfect cell attachment to the fibres and that each cell is only attached to one fibre. All these factors undoubtedly raise the prospect that the reported values of fibre kinematics, i.e. the radius/angle of rotation and the extent of linear displacement, in this study may not be the absolute values experienced by the fibres *in situ*. Nevertheless, it was not the intention of this study to calculate the absolute numerical values of fibre rotation or displacement during the stress-relaxation and creep behaviours. Rather, the primary objective was to show that such kinematics exist. The presented theoretical criterion in this study that links the observed kinematics to stress-relaxation and creep behaviours is independent of the amount of fibre rotation/sliding.

We further note that the analysis presented in this study was devised based on the assumption that the observed kinematics relate only to collagen fibres and not the elastin. Whilst likely a simplification, by its nature the elastin network is unlikely to contribute significantly to viscoelastic behaviour of the AV tissue. Further, Huang and Shadow Huang (2015) have demonstrated that AV samples with decreased collagen content reported significantly altered relaxation behaviour, particularly in terms of trend and modes of relaxation. Therefore, collagen fibres are perhaps the most important fibrous component contributing to the time-dependent behaviour of the AV. A positive improvement in the experimental setup which will be incorporated by the host lab in future studies is to directly visualise the residing collagen fibres within the tissue samples, instead of using the

AVICs as markers of fibre movement. Directly tracking the movement of fibres will obviate many assumptions used in this study, including the nature of attachment of the cells to the fibres.

The utilised theoretical framework for describing the observed kinematics also contained some simplifications such as neglecting the normal component of the traction force, as well as specific assumptions on the interactions of two adjacent fibres. However, the validity of those assumptions and simplifications is corroborated by the affinity of the experimental results and the outcomes of the theoretical analysis, as well as by matching with the tissue-level relaxation and creep behaviours.

6.2. Relevance to the physiological function

The loading/deformation range employed in this study extends beyond the physiological range for AV function *in vivo*. This range was chosen for a more comprehensive biomechanical investigation and characterisation of the micromechanics of AV stress-relaxation and creep. Physiological AV strains reach approximately 10% and 30% in the circumferential and radial directions, respectively, at a stress level of approximately 240 kPa (Sacks and Yoganathan, 2007). From a stress-relaxation perspective, our analysis suggests that if the tissue is to experience relaxation *in vivo*, it will experience two relaxation modes where the rotation of the wavy fibres likely dominates the second relaxation mode (equations $(23)_1$ and $(24)_1$). From the creep mechanics point of view, our analysis offers a clear theoretical explanation as to why under physiological loading boundary condition, the tissue exhibits no creep. These analyses provide new insight into the underlying structural mechanisms that govern the time-dependent behaviour of the AV.

6.3. Possible co-existence of other mechanisms

We note that while we have shown the tissue relaxation and creep behaviours can be described based on the kinematics of the AV microstructure, it may well be the case that other mechanisms at different levels (e.g. fibrillar or molecular hierarchical levels) also co-exist. For example, Gupta et al. (2010) have demonstrated that tendon collagen exhibits stress-relaxation behaviour at fibril level, and Liao et al. (2007) have shown a reduction in collagen fibril D-spacing during relaxation in valvular tissues. While such mechanisms

may co-exist with the microstructural mechanisms established in this study, it is not yet known to what extent they may contribute to tissue-level stress-relaxation and creep behaviours. In addition, these mechanisms have not been analytically linked to the type and number of relaxation modes in soft tissues. Our study, to the knowledge of the authors, is the first to provide a link between the kinematics of the AV microstructure and the observed tissue level relaxation and creep modes.

6.4. Application in modelling the tissue-level behaviour

The mathematical criterion presented in this study was aimed at providing an analytical link between the experimentally observed microstructural reorganisation and the mechanics of AV stress-relaxation and creep. It was not intended to model the tissue-level behaviour, and therefore no tissue-level characteristics such as anisotropy, fibre dispersion, distribution of fibre recruitment or other continuum-based attributes were considered in the presented work. Developing a microstructural model to describe the tissue level stress-relaxation and creep behaviours using the mathematical framework presented here will be a future development. It is noteworthy that while our analysis in this work centred on the AV tissue, the kinematics framework utilised here is generic to planar collagenous soft tissues and may offer insights into modelling the stress-relaxation and creep behaviours of other such tissues.

Appendix A - Deriving the relationship for the traction force *T(x,t)*

Equation (1) reads: $T(x,t) = \pm\mu N(x) + C_d V_{rel}(x,t)$, where $\mu N(x)$ represents the classic Coulomb friction force, and $C_d V_{rel}(x,t)$ is the Newtonian viscous force, whereby C_d becomes the viscous damping coefficient of the ground substance and $V_{rel}(x,t)$ the relative velocity of the fibres sliding against each other.

While in a series of previous studies we have demonstrated that the viscous damping coefficient in AV tissue may be rate dependant itself, indicating that the ground substance may be non-Newtonian (Anssari-Benam et al. 2011b; 2016; 2017), we assume a Newtonian behaviour here for simplicity of the proceeding analysis. The normal force *N* is a function of *x* along the fibre, as the fibres are assumed to have direct contact only at specific regions along their lengths. The same goes for the relative velocity V_{rel}, with an additional caveat that under time-dependent loading, V_{rel} would also generally be a function of time *t*, as the relative movement of two adjacent fibres may not remain uniform in time. The resultant traction force *T* would therefore be a function of both *x* and *t*, $T(x,t)$, *a priori*. We note that if the two adjacent fibres are in direct dry frictional contact, i.e. slide on each other, then the first term in equation (1) will be the dominant force term. If, however, the fibres slip over each other, then the second term in equation (1), i.e. $C_d V_{rel}(x,t)$, will be the dominant contribution to the resultant traction force *T*, as the fibres will still be in contact with the surrounding 'ground substance' matrix.

For fibres to displace along a straight line, as was documented in §3, there needs to exist a force differential between the two ends, acting along the axes of the fibres. For our two adjacent fibres in Figure 5, we assume that a force differential *ΔF* acts on the opposite ends of the two fibres, in opposing directions. We note that the considered configuration is analogous to a case where the fibres are free at one end, i.e. at $x = -l/2$ and $x = l/2$ for fibres 1 and 2, respectively, and loaded at the other end.

For the considered differential elements of the fibres in Figure 5, if the inertial effects are ignored, the condition of equilibrium enforces that *ΔF* must be counterbalanced by the traction force *T(x,t)* acting over the length *dx* of the elements. Therefore, the overall force acting on the whole of the fibre may be calculated as:

$$F(t) = \int_{-\frac{l}{2}}^{\frac{l}{2}} T(x,t)dx \tag{A.1}$$

We note that force F is only a function of time t, as it already accounts for the whole length of the fibre. Moreover, during relaxation, the force acting on each fibre would vary as a function of time. We further note that the global equilibrium of fibres 1 and 2 requires that: $F(t) = F_1(x,t) + F_2(x,t)$, and therefore in light of equation (A.1):

$$F(t) = F_1(x,t) + F_2(x,t) = \int_{-\frac{l}{2}}^{\frac{l}{2}} T(x,t)dx \tag{A.2}$$

Note that F_1 and F_2 are both functions of x and t, as the magnitude of both forces depends on the position (x) along the fibre, as well as the time point (t) during the loading.

When straight, collagen fibres in the AV tissue are assumed to behave as a linear elastic material (e.g. Sacks 2003). Therefore:

$$\frac{F}{A} = E\frac{\partial u}{\partial x} \tag{A.3}$$

where u is the displacement of the material points in the fibre, E is the elastic modulus of the fibre, and A is its cross-sectional area. From equation (A.2), it is evident that $\frac{\partial F(t)}{\partial x} = T(x,t)$. Therefore, equation (A.3) may be re-written as:

$$AE\frac{\partial^2 u(x,t)}{\partial x^2} = T(x,t) \tag{A.4}$$

Applying the above equation to fibres 1 and 2:

$$\begin{cases} A_1 E_1 \dfrac{\partial^2 u_1(x,t)}{\partial x^2} = T(x,t) \\[4mm] A_2 E_2 \dfrac{\partial^2 u_2(x,t)}{\partial x^2} = -T(x,t) \end{cases} \tag{A.5}$$

where A_1 and A_2 are the cross-sectional area, E_1 and E_2 are the elastic moduli, and u_1 and u_2 are the displacements for fibre 1 and fibre 2, respectively. Equation (A.5) describes the displacement fields for the interfacing fibres. Subtracting equation (A.5)$_2$ from (A.5)$_1$, one obtains:

$$AE\left(\frac{\partial^2 u_1(x,t)}{\partial x^2} - \frac{\partial^2 u_2(x,t)}{\partial x^2}\right) = 2T(x,t) \qquad (A.6)$$

In the above equation, we have assumed that the two fibres are geometrically and mechanically uniform, i.e. $A_1 = A_2 = A$ and $E_1 = E_2 = E$.

The accurate nature of contact between neighbouring fibres in the AV tissue is perhaps a topic of debate. It would appear unlikely, however, for adjacent fibres to be in full contact with each other over their entire lateral surface areas. The more two adjacent fibres deviate from full lateral contact over their surface areas, the more the effect of the Coulomb friction term $\mu N(x)$ in equation (1) reduces. Moreover, it would be also unlikely for two adjacent fibres to be in 'dry' contact with each other, as fibres are embedded in a matrix which consists of water and the viscous-like glycosaminoglycans (GAGs) (Anssari-Benam et al. 2011b; 2016; 2017). In a simple description, this matrix mixture 'wets' the surface area of the fibres, which in turn would diminish the effect of μ and thereby the term $\mu N(x)$. Therefore, considering these premises, the contribution of the first term in equation (1) may be considered minimal compared with the second term, and with a degree of tolerance may be discarded from the traction force $T(x,t)$. Therefore, equation (1) may be simplified to:

$$T(x,t) = C_d \frac{\partial}{\partial t}\big(u_1(x,t) - u_2(x,t)\big) \qquad (A.7)$$

Appendix B - Deriving the governing fibre kinematics equation for a wavy fibre

In the considered composite mixture of the ground matrix and wavy fibres shown in Figure 6, the contribution of wavy fibres to the mechanical behaviour when the fibres crimp or uncripm is clearly not to the extent of a fully straight fibre. Thus, the value of the elastic modulus of the composite E_c in equation (10) theoretically falls somewhere between the elastic modulus of the matrix E_m when the fibres do not provide reinforcement at all, and the fraction volume of the fibres V_f multiplied by the elastic modulus of the fibres E when the fibres are fully straight; i.e. $E_m < E_c < V_f E$. It may therefore be reasonable to analytically approximate E_c as a function of E such that: $E_c = \phi E$, where ϕ is a parameter between $0 < \phi < 1$. We further note that the AV tissue matrix is composed of water and GAGs, and therefore is considered incompressible, where $\upsilon = \upsilon_c \to 0.5$. Equation (10) may now be re-written as:

$$\frac{F}{A} = \frac{\phi E}{(1-\upsilon^2)}\left[\frac{\partial u}{\partial x} + \upsilon \frac{\partial u}{\partial y}\right]$$

(B.1)

where it is assumed that the two fibres have uniform mechanical and geometrical properties. In addition, for small uniaxial deformations along x, where the change in the angle between the two adjacent fibres is also small, $\frac{\partial u}{\partial x} \gg \frac{\partial u}{\partial y}$ and $\frac{\partial u}{\partial y} \to 0$. Therefore, equation (B.1) may be simplified to:

$$\frac{F}{A} = \frac{\phi E}{(1-\upsilon^2)}\left[\frac{\partial u}{\partial x}\right]$$

(B.2)

Taking a differential with respect to x from both sides of the above equation, one obtains:

$$\frac{\partial F}{\partial x} = \frac{\phi AE}{(1-\upsilon^2)}\frac{\partial^2 u}{\partial x^2}$$

(B.3)

Equation (B.3) is the counterpart to equation (A.3). Repeating the same steps here as for those from equation (A.3) onward, the governing fibre kinematics equation for wavy fibres may be obtained as:

$$\frac{\phi AE}{(1-\upsilon^2)}\frac{\partial^2}{\partial x^2}u_1(x,t) = 2C_d \frac{\partial}{\partial t}\left(u_1(x,t) - \frac{(1-\upsilon^2)F(t)}{2\phi AE}x\right)$$

(B.4)

Appendix C - Constitutive relationships between stress, strain and time for a generalised 3D transversely isotropic linear viscoelastic Kelvin-Voigt solid

For a Kelvin-Voigt solid under tensile deformation along x direction, the relationship between stress, strain and time reads: $\sigma_x(t) = E_x \varepsilon_x^{axial}(t) + \eta \dot{\varepsilon}_x^{axial}(t)$. In the case of a transversely isotropic material, the following relationships also hold:

$$
\begin{cases}
\upsilon_{xy} = -\dfrac{\varepsilon_y^{transverse\_x}(t)}{\varepsilon_x^{axial}(t)} \Rightarrow \varepsilon_y^{transverse\_x}(t) = -\upsilon_{xy}\varepsilon_x^{axial}(t) \\[4mm]
\upsilon_{xz} = -\dfrac{\varepsilon_z^{transverse\_x}(t)}{\varepsilon_x^{axial}(t)} \Rightarrow \varepsilon_z^{transverse\_x}(t) = -\upsilon_{xz}\varepsilon_x^{axial}(t)
\end{cases}
\tag{C.1}
$$

Assuming that Poisson ratios are independent of time, the above relationships may be differentiated with respect to time to yield:

$$
\begin{cases}
\dot{\varepsilon}_y^{transverse\_x}(t) = -\upsilon_{xy}\dot{\varepsilon}_x^{axial}(t) \\[4mm]
\dot{\varepsilon}_z^{transverse\_x}(t) = -\upsilon_{xz}\dot{\varepsilon}_x^{axial}(t)
\end{cases}
\tag{C.2}
$$

Similarly, for deformation along y direction one gets $\sigma_y(t) = E_y \varepsilon_y^{axial}(t) + \eta \dot{\varepsilon}_y^{axial}(t)$, with:

$$
\begin{cases}
\upsilon_{yx} = -\dfrac{\varepsilon_x^{transverse\_y}(t)}{\varepsilon_y^{axial}(t)} \Rightarrow \varepsilon_x^{transverse\_y}(t) = -\upsilon_{yx}\varepsilon_y^{axial}(t) \Rightarrow \dot{\varepsilon}_x^{transverse\_y}(t) = -\upsilon_{yx}\dot{\varepsilon}_y^{axial}(t) \\[4mm]
\upsilon_{yz} = -\dfrac{\varepsilon_z^{transverse\_y}(t)}{\varepsilon_y^{axial}(t)} \Rightarrow \varepsilon_z^{transverse\_y}(t) = -\upsilon_{yz}\varepsilon_y^{axial}(t) \Rightarrow \dot{\varepsilon}_z^{transverse\_y}(t) = -\upsilon_{yz}\dot{\varepsilon}_y^{axial}(t)
\end{cases}
$$

$$\tag{C.3}$$

And, finally, for deformation along z direction: $\sigma_z(t) = E_z \varepsilon_z^{axial}(t) + \eta \dot{\varepsilon}_z^{axial}(t)$, with:

$$
\begin{cases}
\upsilon_{zx} = -\dfrac{\varepsilon_x^{transverse\_z}(t)}{\varepsilon_z^{axial}(t)} \Rightarrow \varepsilon_x^{transverse\_z}(t) = -\upsilon_{zx}\varepsilon_z^{axial}(t) \Rightarrow \dot{\varepsilon}_x^{transverse\_z}(t) = -\upsilon_{zx}\dot{\varepsilon}_z^{axial}(t) \\[4mm]
\upsilon_{zy} = -\dfrac{\varepsilon_y^{transverse\_z}(t)}{\varepsilon_z^{axial}(t)} \Rightarrow \varepsilon_y^{transverse\_z}(t) = -\upsilon_{zy}\varepsilon_z^{axial}(t) \Rightarrow \dot{\varepsilon}_y^{transverse\_z}(t) = -\upsilon_{zy}\dot{\varepsilon}_z^{axial}(t)
\end{cases}
$$

$$\tag{C.4}$$

Applying the principle of superposition to x direction to compute the total strain $\varepsilon_x(t)$ along x direction, one may obtain:

$$\varepsilon_x(t) = \varepsilon_x^{axial}(t) + \varepsilon_x^{transverse\_y} + \varepsilon_x^{transverse\_z}(t)$$

$$= \frac{\sigma_x(t)}{E_x} - \frac{\eta}{E_x}\dot{\varepsilon}_x^{axial}(t) - \upsilon_{yx}\frac{\sigma_y(t)}{E_y} - \frac{\eta}{E_y}\dot{\varepsilon}_x^{transverse\_y} - \upsilon_{zx}\frac{\sigma_z(t)}{E_z} - \frac{\eta}{E_z}\dot{\varepsilon}_x^{transverse\_z}(t)$$

$$(C.5)$$

For $\dot{\varepsilon}_x(t)$ terms in the above equation, we not that:

$$\text{sum of } \dot{\varepsilon}_x(t) \text{ terms} = \frac{\eta}{E_x}\dot{\varepsilon}_x^{axial}(t) + \frac{\eta}{E_y}\dot{\varepsilon}_x^{transverse\_y} + \frac{\eta}{E_z}\dot{\varepsilon}_x^{transverse\_z}(t) \qquad (C.6)$$

For a transversely isotropic material where the characteristic direction is along x axis, one may note that $E_y = E_z$, and therefore the above reads:

$$\text{sum of } \dot{\varepsilon}_x(t) \text{ terms} = \frac{\eta}{E_x}\dot{\varepsilon}_x^{axial}(t) + \frac{\eta}{E_y}\dot{\varepsilon}_x^{transverse\_y} + \frac{\eta}{E_y}\dot{\varepsilon}_x^{transverse\_z}(t) \qquad (C.7)$$

We further note that: $\dfrac{\upsilon_{xy}}{E_x} = \dfrac{\upsilon_{yx}}{E_y} \Rightarrow E_y = \dfrac{\upsilon_{yx}}{\upsilon_{xy}}E_x$, and therefore equation (C.7) becomes:

$$\text{sum of } \dot{\varepsilon}_x(t) \text{ terms} = \frac{\eta}{E_x}\dot{\varepsilon}_x^{axial}(t) + \frac{\upsilon_{xy}\,\eta}{\upsilon_{yx}\,E_x}\dot{\varepsilon}_x^{transverse\_y} + \frac{\upsilon_{xy}\,\eta}{\upsilon_{yx}\,E_x}\dot{\varepsilon}_x^{transverse\_z}(t) \qquad (C.8)$$

which may be rewritten as:

$$\text{sum of } \dot{\varepsilon}_x(t) \text{ terms} = \frac{\eta\,\upsilon_{xy}}{E_x\,\upsilon_{yx}}\left[\dot{\varepsilon}_x(t) + \frac{(1 - \dfrac{\upsilon_{xy}}{\upsilon_{yx}})\dot{\varepsilon}_x^{axial}(t)}{\dfrac{\upsilon_{xy}}{\upsilon_{yx}}}\right] \qquad (C.9)$$

It may be observed that the term in the bracket may mathematically be considered as a multiple of $\dot{\varepsilon}_x(t)$, say $A\dot{\varepsilon}_x(t)$, and hence equation (C.9) may also be rewritten as:

$$\text{sum of } \dot{\varepsilon}_x(t) \text{ terms} = \frac{\eta\,\upsilon_{xy}}{E_x\,\upsilon_{yx}}\left[A\dot{\varepsilon}_x(t)\right] \qquad (C.10)$$

Therefore, the total strain $\varepsilon_x(t)$ along x direction in equation (C.5) may now be rewritten as:

$$\varepsilon_x(t) = \frac{\sigma_x(t)}{E_x} - \upsilon_{yx}\frac{\sigma_y(t)}{E_y} - \upsilon_{zx}\frac{\sigma_z(t)}{E_z} - \frac{\eta\,\upsilon_{xy}}{E_x\,\upsilon_{yx}}\left[A\dot{\varepsilon}_x(t)\right] \qquad\text{(C.11)}$$

By applying the same procedure to y and z directions, one may obtain the following relationships $\varepsilon_y(t)$ and $\varepsilon_z(t)$ as:

$$\varepsilon_y(t) = \varepsilon_y^{axial}(t) + \varepsilon_y^{transverse\_x} + \varepsilon_y^{transverse\_z}(t) = \frac{\sigma_y(t)}{E_y} - \upsilon_{xy}\frac{\sigma_x(t)}{E_x} - \upsilon_{zy}\frac{\sigma_z(t)}{E_z} - \frac{\eta}{E_y}\left[B\dot{\varepsilon}_y(t)\right]$$

$$\text{(C.12)}$$

and:

$$\varepsilon_z(t) = \varepsilon_z^{axial}(t) + \varepsilon_z^{transverse\_x} + \varepsilon_z^{transverse\_y}(t) = \frac{\sigma_z(t)}{E_z} - \upsilon_{xz}\frac{\sigma_x(t)}{E_x} - \upsilon_{yz}\frac{\sigma_y(t)}{E_y} - \frac{\eta}{E_z}\left[C\dot{\varepsilon}_z(t)\right]$$

$$\text{(C.13)}$$

In view of equations (C.11), (C.12) and (C.13), the constitutive relationships between stress, strain and time for a generalised 3D transversely isotropic linear viscoelastic Kelvin-Voigt solid may be given by:

$$\begin{cases} \varepsilon_x(t) = \dfrac{\sigma_x(t)}{E_x} - \upsilon_{yx}\dfrac{\sigma_y(t)}{E_y} - \upsilon_{zx}\dfrac{\sigma_z(t)}{E_z} - \dfrac{\eta\,\upsilon_{xy}}{E_x\,\upsilon_{yx}}\left[A\dot{\varepsilon}_x(t)\right] \\[4mm] \varepsilon_y(t) = \dfrac{\sigma_y(t)}{E_y} - \upsilon_{xy}\dfrac{\sigma_x(t)}{E_x} - \upsilon_{zy}\dfrac{\sigma_z(t)}{E_z} - \dfrac{\eta}{E_y}\left[B\dot{\varepsilon}_y(t)\right] \\[4mm] \varepsilon_z(t) = \dfrac{\sigma_z(t)}{E_z} - \upsilon_{xz}\dfrac{\sigma_x(t)}{E_x} - \upsilon_{yz}\dfrac{\sigma_y(t)}{E_y} - \dfrac{\eta}{E_z}\left[C\dot{\varepsilon}_z(t)\right] \end{cases} \qquad\text{(C.14)}$$

References

Alavi, S.H., Ruiz, V., Krasieva, T., Botvinick, E.L., Kheradvar, A., 2013. Characterizing the collagen fiber orientation in pericardial leaflets under mechanical loading conditions. Ann. Biomed. Eng. 41, 547-561.

Anssari-Benam, A., 2014. Is the time-dependent behaviour of the aortic valve intrinsically quasi-linear? Mech. Time-Depend. Mater. 18, 339-348.

Anssari-Benam, A., Bader, D.L., Screen, H.R.C., 2011a. Anisotropic time-dependant behaviour of the aortic valve. J. Mech. Behav. Biomed. Mater. 4, 1603-1610.

Anssari-Benam, A., Bader, D.L., Screen, H.R.C., 2011b. A combined experimental and modelling approach to aortic valve viscoelasticity in tensile deformation. J. Mater. Sci. Mater. Med. 22, 253-262.

Anssari-Benam, A., Barber, A.H., Bucchi, A., 2016. Evaluation of bioprosthetic heart valve failure using a matrix-fibril shear stress transfer approach. J. Mater. Sci. Mater. Med. 27, 42.

Anssari-Benam, A., Bucchi, A., 2018. Modeling the deformation of the elastin network in the aortic valve. J. Biomech. Eng. 140; doi: 10.1115/1.4037916.

Anssari-Benam, A., Bucchi, A., Bader, D.L., 2015. Unified viscoelasticity: Applying discrete element models to soft tissues with two characteristic times. J. Biomech. 48, 3128-3134.

Anssari-Benam, A., Bucchi, A., Screen, H.R.C., Evans, S.L., 2017. A transverse isotropic viscoelastic constitutive model for aortic valve tissue. R. Soc. Open Sci. DOI: 10.1098/rsos.160585.

Anssari-Benam, A., Gupta, H.S., Screen, H.R.C., 2012. Strain transfer through the aortic valve. J. Biomech. Eng. 134, 061003.

Anssari-Benam, A, Tseng, Y.-T., Bucchi, A., 2018. A transverse isotropic constitutive model for the aortic valve tissue incorporating rate-dependency and fibre dispersion: Application to biaxial deformation. J. Mech. Behav. Biomed. Mater. 85: 80-93.

Billiar, K.L., Sacks, M.S., 2000. Biaxial mechanical properties of the native and glutaraldehyde-treated aortic valve cusp: Part II - A structural constitutive model. J. Biomech. Eng. 122: 327-335.

Carslaw, H.S., Jaeger, J.C., 1959. Conduction of heat in solids. 2nd Edition, Oxford University Press, London, UK.

Gupta, H.S., Seto, J., Krauss, S., Boesecke, P., Screen, H.R.C., 2010. In situ multi-level analysis of viscoelastic deformation mechanisms in tendon collagen. J. Struct. Biol. 169, 183-191.

Huang, S., Shadow Huang, H.-Y., 2015. Biaxial stress relaxation of semilunar heart valve leaflets during simulated collagen catabolism: Effects of collagenase concentration and equibiaxial strain state. Proc. Inst. Mech. Eng. H 229, 721-731.

Kojic, M., Mijailovic, S., Zdravkovic, N., 1998. A numerical algorithm for stress integration of a fiber-fiber kinetics model with Coulomb friction for connective tissue. Comput. Mech. 21, 189-198.

Lewinsohn, A.D., Anssari-Benham, A., Lee, D.A., Taylor, P.M., Chester, A.H., Yacoub, M.H., Screen, H.R.C., 2011. Anisotropic strain transfer through the aortic valve and its relevance to the cellular mechanical environment. Proc. Inst. Mech. Eng. H 225, 821-830.

Liao, J., Yang, L., Grashow, J., Sacks, M.S., 2007. The relation between collagen fibril kinematics and mechanical properties in the mitral valve anterior leaflet. J. Biomech. Eng. 129, 78-87.

Meng. X., Ao, L., Song, Y., Babu, A., Yang, X., Wang, M., Weyant, M.J., Dinarello, C.A., Cleveland, J.C. Jr, Fullerton, D.A., 2008. Expression of functional Toll-like receptors 2 and 4 in human aortic valve interstitial cells: potential roles in aortic valve inflammation and stenosis. Am. J. Physiol. Cell. Physiol. 294, C29-C35.

Mijailovich, S.M., Stamenovic, D., Fredberg, J.J., 1993. Toward a kinetic theory of connective tissue micromechanics. J. Appl. Physiol. 74, 655-681.

Mow, V.C., Mak, A.F., Lai, W.M., Rosenberg, L.C., Tang, L.H., 1984. Viscoelastic properties of proteoglycan subunits and aggregates in varying solution concentrations. J. Biomech. 17, 325-338.

Nielsen, L.E., Landel, R.F., 1994. Mechanical properties of polymers ad composites. 2nd Edition, Marcel Dekker, New York, USA, pp. 116-117.

Robinson, P.S., Tranquillo, R.T., 2009. Planar biaxial behavior of fibrin-based tissue-engineered heart valve leaflets. Tissue Eng. Part A 15, 2763-2772.

Rock, C.A., Han, L., Doehring, T.C., 2014. Complex collagen fiber and membrane morphologies of the whole porcine aortic valve. PloS One 21, 9. doi: 10.1371/journal.pone.0086087.

Sacks, M.S., 2001. The biomechanical effects of fatigue on the porcine bioprosthetic heart valve. J. Long Term Eff. Med. Implants 11, 231-247.

Sacks, M.S., 2003. Incorporation of experimentally-derived fiber orientation into a structural constitutive model for planar collagenous tissues. J. Biomech. Eng. 125, 280-287.

Sacks, M.S., Yoganathan, A.P., 2007. Heart valve function: a biomechanical perspective. Philos. Trans. R. Soc. Lond. B Bio. Sci. 362, 1369-1391.

Sauren, A.A., van Hout, M.C., van Steenhoven, A.A., Veldpaus, F.E., Janssen, J.D., 1983. The mechanical properties of porcine aortic valve tissues. J. Biomech. 16, 327-337.

Shadow Huang, H.-Y., Liao, J., Sacks, M.S., 2007. In-situ deformation of the aortic valve interstitial cell nucleus under diastolic loading. J. Biomech. Eng. 129, 880-889.

Stella, J.A., Liao, J., Sacks, M.S., 2007. Time-dependent biaxial mechanical behavior of the aortic heart valve leaflet. J. Biomech. 40, 3169-3177.

Tan, T., Cholewa, N.M., Case, S.W., De Vita, R., 2016. Micro-structural and biaxial creep properties of the swine uterosacral–cardinal ligament complex. Ann. Biomed. Eng. 44, 3225-3237.

Zhu, W., Iatridis, J.C., Hlibczuk, V., Ratcliffe, A., Mow, V.C., 1996. Determination of collagen-proteoglycan interactions in vitro. J. Biomech. 29, 773-783.

Table legends

Table 1 - Modes of stress-relaxation and creep phenomena and the dominant kinematics of the microstructure at each strain/load level. Data reported from Anssari-Benam et al. 2011a.

Table 1

	Stress-relaxation				
	Circumferential direction			**Radial direction**	
Strain level	**No. of decay mode(s)**	**Dominant kinematics**		**No. of decay mode(s)**	**Dominant kinematics**
$\varepsilon < 6\%$	1	No kinematics		1	No kinematics
$6\% \leq \varepsilon \leq 12\%$	2	Curvilinear		1	No kinematics
$\varepsilon > 12\%$	2	Linear displacement		1	No kinematics
	Creep				
	Circumferential direction			**Radial direction**	
Load level	**Creep mode(s)**	**Dominant kinematics**		**Creep mode(s)**	**Dominant kinematics**
$f \leq 1.5\,\text{N}$	P & S	Curvilinear		P & S	Not established
$f > 1.5\,\text{N}$	P & S	Linear displacement		P & S	Not established

Figure legends

Figure 1 - (a) AV leaflets were excised from the aortic root, from which 5mm wide strips were cut from the belly region, in either the circumferential or radial direction (adapted from Anssari-Benam et al. 2016); (b) A typical confocal microscopy image of AVIC nuclei stained with Acridine Orange. For structural comparison, images of AV fibrous structure (collagen fibres and the elastin network) have also been presented at the same length-scale within the same size field of view. AVICs are known to be bonded to the fibres; (c) A schematic of the integrated setup used to quantify the kinematics of AV microstructural reorganisation, including a photograph of the loading rig on the stage of the microscope.

Figure 2 - Schematics depicting methods for describing the movement of the nuclei. The trajectory of movement of each nucleus is reconstructed from each captured frame: (a) A typical trajectory of movement of a nucleus during a 300s test at lower force/strain levels where the dominant kinematic is a curvilinear motion. The equation of a circle is curve-fitted to the trajectory curve, from which the radius of curvature of the trajectory is determined. Note that the top right panel is a magnification of the real trajectory for better presentation and the axes are not to the same scale; (b) A typical trajectory of movement of a nucleus during a 300s test at higher force/strain levels where the dominant kinematic is a straight-line motion. The trajectory is described by a line of best fit ($R^2 \geq 0.98$). The displacement of the nucleus along its direction of movement is then calculated. Note that the scale bars represents 100 μm and the loading direction is along the y axis.

Figure 3 - Typical movement of cell nuclei during stress-relaxation in the circumferential direction: (a) dominant curvilinear motion at strain levels $6\% \leq \varepsilon \leq 12$; and (b) dominant straight-line motion for $\varepsilon \geq 14\%$. No detectable movement in lower strain levels ($\varepsilon < 6\%$) was observed. Dotted lines represent the best line of fit ($R^2 \geq 0.98$) to the recorded trajectory; (c) The mean values of radius of curvature and the linear displacement of the cell nuclei motion at each strain increment. The values are presented as mean ± SD.

Figure 4 - Typical movement of the cell nuclei during creep in the circumferential direction: (a) at load levels $f < 1.5N$, the motion of the nuclei conforms with a curvilinear motion and the trajectory of movement is characterised as a segment of the circumference of a circle. At $f = 1.5N$, the transition of the cell nuclei motion from curvilinear to straight-

line kinematics is documented; (b) at load levels $f > 1.5N$, the dominant kinematics is the straight-line motion. Dotted lines represent the best line of fit; (c) The mean values of radius of curvature and the linear displacement of the cell nuclei motion at each load increment. The values are presented as mean ± SD.
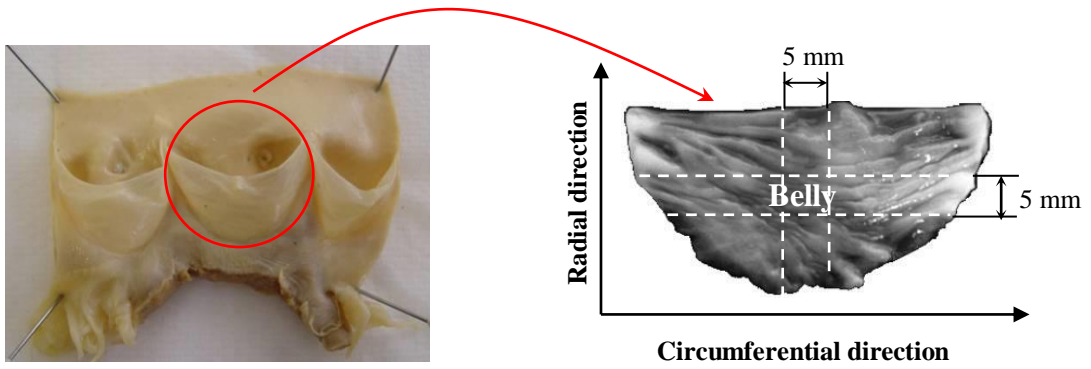
Figure 5 - Schematic of the fibre kinematics of two arbitrary adjacent straight collagen fibres (adapted from Kojic et al. 1998).

Figure 6 - Schematic of two adjacent wavy fibres embedded in the matrix, at the beginning ($t = 0s$) and the end ($t = 300s$) of a test. The fibres may rotate and change their lengths as part of the microstructural reorganization occurring within the tissue during stress-relaxation/creep phenomena.
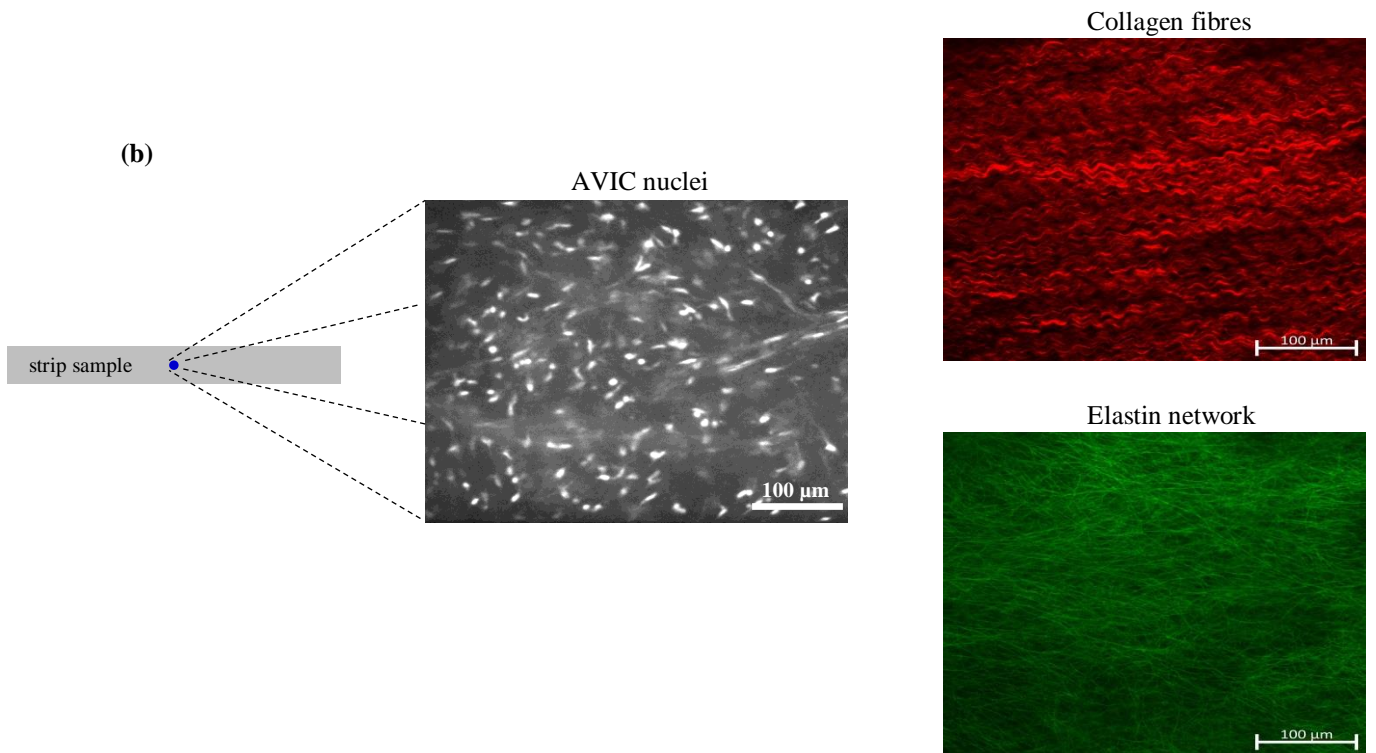
Figure 7 - Comparison of uniaxial versus equi-biaxial creep in circumferential and radial directions using the AV mechanical properties as reported by Stella et al. 2007. Continuous and dashed lines represent the equi-biaxial and uniaxial creep behaviours, respectively.
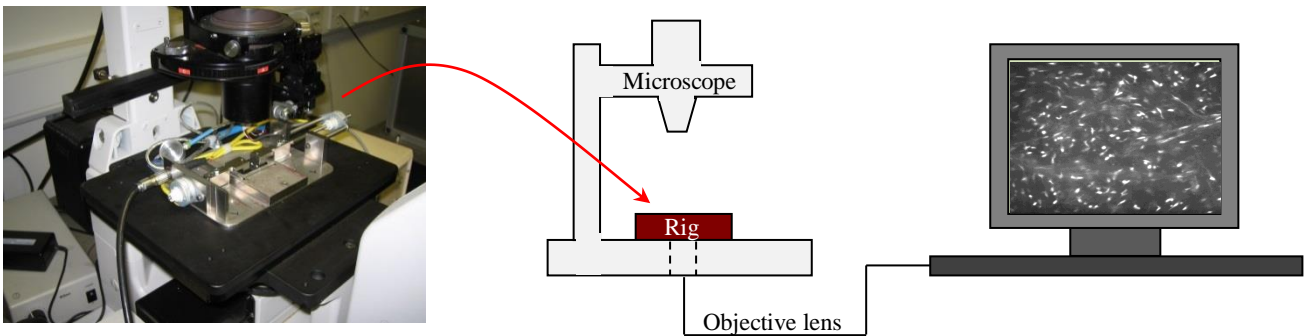
Figure 1

(a)

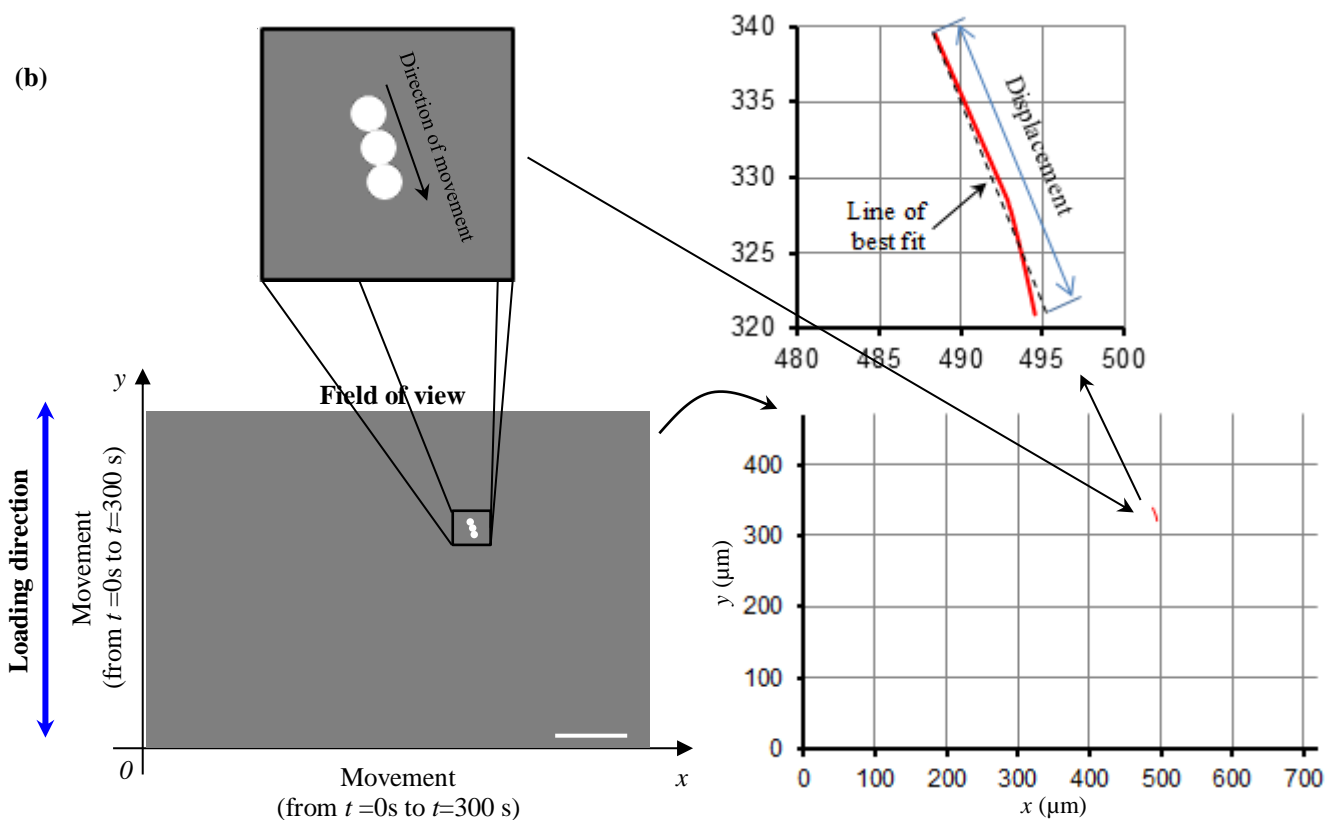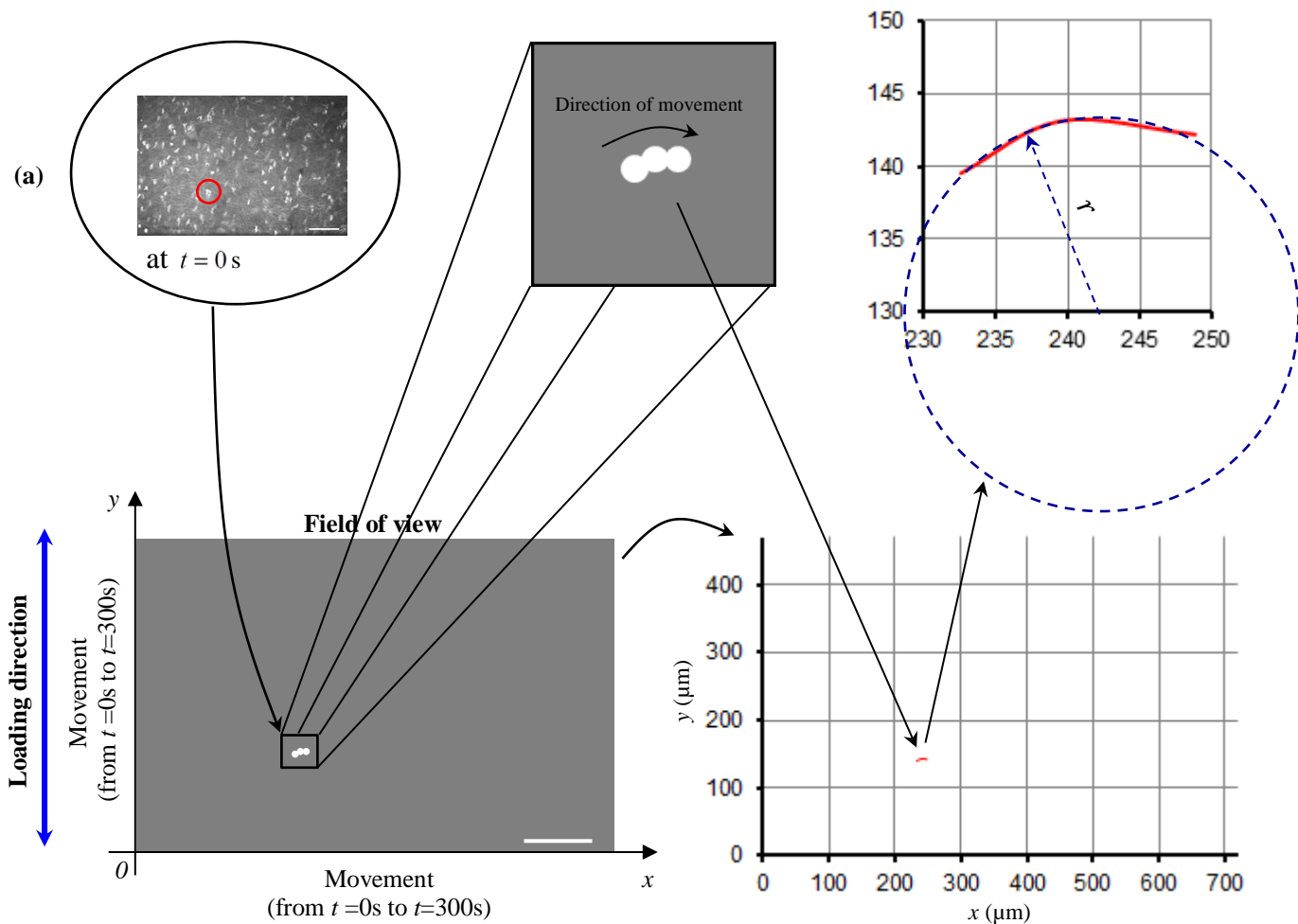**5 mm**

Radial direction

Belly

5 mm

Circumferential direction

(b)

Collagen fibres

AVIC nuclei

strip sample

100 µm

100 µm

Elastin network

100 µm

(c)

Microscope

Rig

Objective lens

Figure 2

43

Figure 3

Figure 4

Figure 5

Tissue sample

$F_{external}$

l

Fibre 1

F_1

$F_2 + \Delta F$

$F_1 + \Delta F$

F_2

$F_{external}$

Fibre 2

dx

$F_1 \longleftarrow \text{ } \longrightarrow F_1 + \dfrac{\partial F_1}{\partial x}\,dx$

$T(x,t)$

$F_2 + \dfrac{\partial F_2}{\partial x}\,dx \longleftarrow \text{ } \longrightarrow F_2$

x

$-\dfrac{l}{2}$

0

$\dfrac{l}{2}$

$F(t)$

$F(t)$

Figure 6

at $t = 0$s

$\mathbf{F_{ext}(t)}$

$\mathbf{F_{ext}(t)}$

at $t = 300$s

$\mathbf{F_{ext}(t)}$

$\mathbf{F_{ext}(t)}$

x

Figure 7